

## An Inverse Optimization Approach Toward Testing Different Hypotheses of Vascular Homeostasis Using Image-based Models

S. Zeinali-Davarani<sup>1</sup>, L. G. Raguin<sup>1,2</sup>, S. Baek<sup>1</sup>

<sup>1</sup>Departments of Mechanical Engineering and <sup>2</sup>Radiology,  
Michigan State University, East Lansing, MI 48824, U.S.A

---

### Abstract

Vascular mechanical homeostasis is a fundamental assumption in modeling vascular growth and remodeling. Meanwhile, it is a matter of debate, which mechanical quantity is responsible for governing the vascular growth and remodeling process. Recently, an optimization method has been proposed to estimate the optimal distributions of arterial wall thickness and anisotropy, such that a homeostatic condition is satisfied. In this study, the same optimization technique is utilized to investigate variations in the distribution of wall thickness and anisotropy due to different homeostatic assumptions, while two geometric models, one from a healthy aorta and one from a healthy internal iliac artery, are independently used. Prior to optimization, material constitutive parameters are estimated by fitting biaxial mechanical test data from human aorta and prescribed into the optimization process. Objective functions are set to restore both the original arterial geometry and the homeostatic state based on either intramural stress or cyclic circumferential stretch. Different homeostatic assumptions lead to distinct results for the optimal distributions of wall thickness and anisotropy. Namely, the cyclic stretch homeostatic assumption yields lower levels of the wall thickness as well as a less longitudinal variation of anisotropy. However, the arterial wall is consistently found to be thicker on the concave regions rather than on the convex regions. With further improvements in the application of the boundary conditions, the presented computational method seems promising to enhance our understanding of the vascular mechanical homeostasis and shall serve as a basis for conducting validation experiments.

*Key words:* Patient-specific modeling; Vascular mechanics; Inhomogeneous properties; Growth and remodeling; Parameter estimation

---

### 1. Introduction

In their seminal paper, Humphrey and Rajagopal (2002) introduced a new theoretical framework, called a constrained mixture model for modeling growth and remodeling (G&R) of soft tissues. They presented a modeling framework that utilizes ideas from classical mixture and homogenization theories while avoiding the technical difficulties associated with mixture theory. This allows the model to capture the complexity that occurs during soft tissue G&R such as deposition of multiple structural components (e.g., fibrous collagen, elastin, and smooth muscle cells) with different natural configurations and turnover rates, whereas the governing equation can be solved as if the soft tissue were made of a single constituent. Often not mentioned, but another important contribution of their paper is the philosophy and guidance in developing a model of G&R of biological tissues, summarized in six remarks in the paper. Based on their pioneering work, during the past decade, many

---

<sup>1</sup>Corresponding author. *Email:* sbaek@egr.msu.edu

constrained mixture models have been developed in the studies of vascular mechanics (Hansen et al., 2009; Gleason et al., 2004; Valentín et al., 2009; Wan et al., 2010), progression of cardiovascular diseases (Baek et al., 2006, 2007; Figueroa et al., 2009; Gleason and Humphrey, 2004; Sheidaei et al., 2011; Zeinali-Davarani et al., 2011b) and mechanosensitive cellular behavior (Humphrey et al., 2008; Hsu et al., 2009).

While most studies after Humphrey and Rajagopal (2002) have focused on modeling the evolution of biological or engineered tissues after the alteration of physiological and pathological conditions, in this paper we study one of the most fundamental, but often overshadowed, assumption that soft tissue has an optimal structure during the maintenance or normal G&R period. Humphrey and Rajagopal (2002) stated in Remark 2.3 that “Normal growth and remodeling tends to be a stable dynamical process, one that seeks to optimize structure and function with respect to yet unidentified parameters.” They further stated that “Although one ultimately seeks parameters that govern the underlying mechanisms of mechanotransduction, it will be sufficient for certain modeling purposes to identify parameters that simply correlate well with the overall process.”

The question that has long been asked and is yet to be answered in biomechanics research is what are the parameters that correlate well with the G&R process? Are they stress, strain, or strain rate that cells respond to? Humphrey (2001) claimed that the question may be ill-posed. Stress and strain are merely convenient mathematical concepts and are not unique observable or physical quantities. He suggested, however, that “the concepts of stress and strain will continue to be convenient metrics in both empirical correlations and phenomenological constitutive relations that seek to relate certain cellular responses to particular stimuli.” A practical question still remains as to what are the constitutive relations for such mechanical quantities, that best describe the maintenance of vascular tissues. During the maintenance, the turnover of cells and extracellular matrix is balanced and unchanged; hence, there is no net change in mass, structure, or the properties. Therefore, it is plausible that we may find the right constitutive relation or at least discriminate between different constitutive relations by numerically investigating the consequence of the constitutive relation in tissue structures and comparing the results with experimental studies. Stress and strain are interrelated (Humphrey, 2001; Kassab, 2008), and using an idealized symmetric model, such as a straight tube, it may be difficult to distinguish the difference in optimal structures obtained from different hypotheses.

In this paper, we propose that in medical image-based models different hypotheses for a mechanical homeostatic state may lead to distinct consequences with regard to the distributions of wall thickness and anisotropy, giving us the opportunity to better understand the governing rules of tissue adaptation. Toward this end, we employ an inverse optimization method that we recently developed to estimate material and structural parameters of image-based models of arteries corresponding to a given constitutive relation (Zeinali-Davarani et al., 2011a), and compare the results with regard to multiple hypotheses of a homeostatic condition.

## 2. Hypotheses on vascular mechanical homeostasis

Vascular tissue tends to adapt in response to changes in its mechanical environment and a variety of evidence offers diverse hypotheses on this homeostatic tendency. In response to a sustained pressure increase, the thickness of the blood vessel increases, implying a tendency toward uniformity of circumferential stress (Matsumoto and Hayashi, 1994; Wolinsky, 1971; Xu et al., 2000). Blood vessel diameter increases in response to an increase in blood flow, thereby normalizing the wall shear stress (Kamiya and Togawa, 1980; Langille et al., 1989). Some studies underscore the importance of strain mechanosensitivity along the coronary arterial tree (Guo and Kassab, 2004; Lu et al., 2001), whereas others indicate strain rate as an important component of vascular homeostasis (McKnight and Frangos, 2003). Meanwhile, the vascular system is under pulsatile forces and several observations emphasize the role of pulsatility in vascular homeostasis (Cummins et al., 2007; Leung et al., 1976). In an *in vivo* study, Eberth et al. (2009) observed a strong correlation between morphology and pulsatility of pressure and flow rather than mean values, which is consistent with a study by Boutouyrie et al. (1999).

Stress and strain are both tensorial quantities and previous studies have sought simpler scalar measures of mechanical stimuli for modeling vascular adaptation. For example, Baek et al. (2006) utilized the magnitude of traction on the plane normal to the fiber direction as a scalar measure of the fiber stress. In another stress-driven model, Hariton et al. (2007) and Driessen et al. (2008) used the normal component of traction on the plane normal to the fiber direction as the remodeling stimulus. These models assumed that the mechanical

stimuli that vascular cells sense correlate with tension or shear on the fibrous tissue that they reside on. The stretch of collagen fibers was also used by Watton and Hill (2009) as the mechanical quantity governing the G&R. Nevertheless, these studies assumed that fibers have the same mechanical properties and, hence, the uniform stretch of fibers means the uniform tension.

In a more phenomenological study, Guo and Kassab (2004) examined the distributions of circumferential stress and strain along the porcine aorta and the coronary arterial tree. They found that the circumferential stretch ratio (from the zero-stress state to the loaded state) is relatively uniform compared to the stress and suggested that the vascular system closely regulates the degree of deformation. It is difficult, however, to explain how the cells in vascular tissues can regulate the deformation given that cells do not experience the zero-stress state of the blood vessel *in vivo*. Lillie and Gosline (2007) suggested that the strain of elastin during the cardiac cycle is nearly constant along the porcine thoracic aorta. Our recent study with the porcine thoracic aorta also showed that the cyclic strain during the cardiac cycle is relatively uniform in the circumferential direction compared to the circumferential component of stress (Kim and Baek, 2011).

In this study, we choose the following three scalar measures that have been proposed in the literature to be associated with the homeostatic state:

- Case 1:  $\sigma^k = \|\boldsymbol{\sigma}^k \mathbf{n}\|$
- Case 2:  $\sigma^k = \mathbf{n} \cdot \boldsymbol{\sigma}^k \mathbf{n}$
- Case 3:  $\lambda^{cyc} = \lambda_1^{sys} / \lambda_1^{dias}$ ,

where  $\boldsymbol{\sigma}^k$  and  $\mathbf{n}$  are the partial stress and the unit vector representing the alignment of the  $k^{th}$  constituent.  $\lambda_1^{sys}$  and  $\lambda_1^{dias}$  are circumferential stretches at systolic and diastolic pressures. The distributions of thickness and fiber alignment are obtained by an inverse optimization using the above three cases.

### 3. Constitutive relations and an inverse optimization method

To identify *in vivo* material and geometric parameters for each case of a homeostatic condition, we follow an inverse optimization method developed by Zeinali-Davarani et al. (2011a) as a two-step procedure; first, estimating constitutive parameters of a healthy human artery using experimental data and, second, estimating the distributions of wall thickness and fiber alignment using an inverse optimization integrated with the finite element model of inflated blood vessels.

#### 3.1. Constitutive equations and material parameters

Here, we briefly describe the constitutive relations. The arterial wall is assumed to be a mixture of constituents ‘ $i$ ’ such as elastin ( $i = e$ ), multiple collagen families ( $i = 1, \dots, k, \dots, 4$ ), and smooth muscle ( $i = m$ ). The strain energy of the mixture per unit reference area is  $w = \sum_i w^i = w^e + \sum_k w^k + w^m + w_{act}^m$  and the membrane stress is given as (Baek et al., 2006; Humphrey, 2002)

$$\mathbf{T} = \frac{2}{J} \mathbf{F} \frac{\partial w}{\partial \mathbf{C}} \mathbf{F}^T, \quad (1)$$

where  $J$  is the determinant of the 2-D deformation gradient  $\mathbf{F}$  and  $\mathbf{C} = \mathbf{F}^T \mathbf{F}$ . The stretches of the smooth muscle (SM) and collagen fiber ‘ $k$ ’ from their natural (stress-free) configuration to the current configuration are given as

$$\lambda_n^k = G_h^c \lambda^k, \quad \lambda_n^m = G_h^m \lambda_1, \quad (2)$$

where  $G_h^m$  and  $G_h^c$  are homeostatic stretches of SM and collagen. We define a new tensor,  $\tilde{\mathbf{G}}^e = \text{diag} \left\{ G_1^e, G_2^e, \frac{1}{G_1^e G_2^e} \right\}$ , which represents a mapping from the natural configuration of elastin to the reference configuration such that,

$$\mathbf{F}_n^e = \mathbf{F} \tilde{\mathbf{G}}^e, \quad \mathbf{C}_n^e = \mathbf{F}_n^{eT} \mathbf{F}_n^e = [\tilde{\mathbf{G}}^e]^T \mathbf{C} \tilde{\mathbf{G}}^e. \quad (3)$$

Table 1: Summary of material parameters used in the optimization.

Elastin:	$c_1 = 50.6 \text{ Nm/kg}$ , $G_1^e = 1.22$ , $G_2^e = 1.23$ , $\nu^e = 0.2$ .
Collagen:	$c_2 = 3195 \text{ Nm/kg}$ , $c_2^{(comp)} = 0.1c_2$ , $c_3 = 25.0$ , $G_h^c = 1.034$ , $\sigma_h^c = 143 \text{ kPa}$ , $\nu^k = [0.06, 0.06, 0.24, 0.24]$ , $\alpha^k = [0^\circ, 90^\circ, 45^\circ, 135^\circ]$ .
Smooth muscle:	$c_4 = 16.45 \text{ Nm/kg}$ , $c_5 = 14.14$ , $G_h^m = 1.165$ , $\nu^m = 0.2$ , $\sigma_h^m = 81 \text{ kPa}$ , $\lambda_M = 1.4$ , $\lambda_0 = 0.8$ , $S = 54 \text{ kPa}$ .
Homeostatic cyclic stretch:	$\lambda_h^{cyc} = 1.02$ .
Density:	$\rho = 1050 \text{ kg/m}^3$ .

Strain energies of the constituents  $i$  per unit reference area,  $w^i$ , are given as

$$w^e(\mathbf{C}_n^e(t)) = M^e \frac{c_1}{2} \left( C_{n[11]}^e + C_{n[22]}^e + \frac{1}{C_{n[11]}^e C_{n[22]}^e - C_{n[12]}^e{}^2} - 3 \right) \quad (4)$$

$$w^k(\lambda_n^k) = M^k \frac{c_2}{4c_3} \left\{ \exp \left[ c_3 ((\lambda_n^k)^2 - 1)^2 \right] - 1 \right\} \quad (5)$$

$$w^m(\lambda_n^m) = M^m \frac{c_4}{4c_5} \left\{ \exp \left[ c_5 ((\lambda_n^m)^2 - 1)^2 \right] - 1 \right\} \quad (6)$$

$$w_{act}^m = M^m \frac{S}{\rho} \left\{ \lambda_1 + \frac{1}{3} \frac{(\lambda_M - \lambda_1)^3}{(\lambda_M - \lambda_0)^2} \right\}, \quad (7)$$

where  $M^i$  is the mass per unit reference area for the constituent  $i$ .  $C_{n[11]}^e$ ,  $C_{n[22]}^e$  and  $C_{n[12]}^e$  are components of  $\mathbf{C}_n^e$ .  $\lambda_M$  and  $\lambda_0$  are stretches at which the SM contraction is maximum and at which active force generation ceases,  $S$  is the stress at the maximum contraction of SM.

Material parameters (summarized in Table 1) are determined in three different ways. The first set of parameters are prescribed from the literature such as density ( $\rho$ ), mass fraction of constituents ( $\nu^i$ ) and ( $\lambda_0$ ,  $\lambda_M$ ,  $S$ ). The second set of parameters ( $c_1$ ,  $c_2$ ,  $c_3$ ,  $c_4$ ,  $c_5$ ,  $G_1^e$ ,  $G_2^e$ ,  $G_h^c$ ,  $G_h^m$ ) are estimated via a nonlinear least squares optimization, proposed by Zeinali-Davarani et al. (2009) using the biaxial mechanical test data of healthy human aorta (Vande Geest et al., 2004, 2006). Subsequently, the target homeostatic values ( $\sigma_h^m$ ,  $\sigma_h^c$ ,  $\lambda_h^{cyc}$ ) are calculated assuming an idealized geometry.

### 3.2. An inverse optimization method

The next step is to estimate the distributions of wall thickness and material anisotropy as an inverse optimization problem where the objective function comprises two additive terms; the first term (“ $\mathcal{EG}$ ”) corresponds to the deviation of geometry from the *in vivo* configuration and the second one (“ $\mathcal{ES}$ ”) corresponds to the deviation of a mechanical state from the homeostatic condition. The first term stems from the fact that a geometry based on medical images is normally considered as the stress-free configuration, while under the *in vivo* pressure it may no longer coincide with the *in vivo* configuration. In this regard, multiple computational approaches have been developed in order to account for the pre-stressed state of vessels in patient-specific computational models (Lu et al., 2007; Gee et al., 2009; de Putter et al., 2007; Speelman et al., 2009). However, these studies do not take into account the optimal structure in vascular homeostasis. The second term of the objective function enforces

the homeostatic condition throughout the domain. Since we are interested in minimizing both terms, each term is normalized and a weight parameter  $\xi$  (or a Lagrange multiplier) is used to adjust the minimization weight for each normalized term. Then, in Cases 1 and 2, the objective function is given as

$$W = \frac{\int_{\Omega} \|\mathbf{x}(h, \alpha^k) - \mathbf{X}_{image}\|^2 dA}{\int_{\Omega} \|\mathbf{X}_{image} - \bar{\mathbf{X}}\|^2 dA} + \xi \sum_i \frac{\nu^i \int_{\Omega} (\sigma^i(h, \alpha^k) - \sigma_h^i)^2 dA}{\int_{\Omega} (\sigma_h^i)^2 dA}, \quad (8)$$

where  $i = m, 1, \dots, k$  and  $\mathbf{x}$  is the finite element (FE) solution for the nodal position vector (see Appendix for details of the image-based FE model of the arterial wall).  $\mathbf{X}_{image}$  constitutes the target geometry and is the nodal position vector of the FE mesh that is generated based on the 3-D models of arteries. The geometric models of arteries are reconstructed from MRI images of normal arteries and assumed to be under mean pressure (see Sheidaei et al. (2011)).  $\bar{\mathbf{X}}$  is the geometric center of the artery and is used as a fixed reference point for normalizing the first term.  $\sigma_h^i$  and  $\nu^i$  are the homeostatic stress and mass fraction assumed for the constituent  $i$ .  $(h, \alpha^k)$  are the unknown wall thickness and anisotropy, i.e. orientation of the collagen fiber  $k$ . The deviation of stress for each constituent is scaled by its mass fraction and integrated over the computational domain. Therefore, constituents such as fiber families in helical directions will be given more weight in minimizing the objective function (see Table 1).

Similarly, the corresponding objective function to minimize in Case 3 is defined as

$$W = \frac{\int_{\Omega} \|\mathbf{x}(h, \alpha^k) - \mathbf{X}_{image}\|^2 dA}{\int_{\Omega} \|\mathbf{X}_{image} - \bar{\mathbf{X}}\|^2 dA} + \xi \frac{\int_{\Omega} (\lambda^{cyc}(h, \alpha^k) - \lambda_h^{cyc})^2 dA}{\int_{\Omega} (\lambda_h^{cyc})^2 dA}, \quad (9)$$

where  $\lambda^{cyc}$  is the cyclic stretch in the circumferential direction. Thickness and anisotropy distributions are then approximated, independently from the finite element mesh, with a smaller (I) number of unknown variables with associated base functions

$$h(s, \theta) = \sum_{j=1}^I \{\beta_j^h \phi_j(s, \theta)\}, \quad \alpha^k(s, \theta) = \sum_{j=1}^I \{\beta_j^k \psi_j(s, \theta)\}, \quad (10)$$

where  $(\beta_j^h, \beta_j^k)$  are variables for thickness and anisotropy associated with the approximation point  $j$ .  $\phi_j(s, \theta)$  and  $\psi_j(s, \theta)$  are basis/approximation functions defined on the computational domain  $\Omega$ , where  $(s, \theta)$  are two spatial parameters that parameterize the arterial wall surface such that  $s$  represents the longitudinal distance along the artery and  $\theta$  represents azimuthal position on the arterial wall (see Zeinali-Davarani et al. (2011a) for more details of this mapping technique). Products of Legendre polynomials ( $P_m; m = 0, \dots, M - 1$ ) and periodic functions ( $F_n; n = 0, \dots, N - 1$ ) are employed for both  $\phi_j$  and  $\psi_j$  (Zeinali-Davarani et al., 2011a).  $M$  and  $N$  determine the total number of optimization variables ( $2I$ ) such that  $I = M \times N$ . The Nelder-Mead simplex algorithm (Lagarias et al., 1998) is implemented to minimize Eqs. (8) and (9) with an appropriate stopping criterion (Torczon, 1989; Zeinali-Davarani et al., 2011a).

#### 4. Results

Two 3-D geometric models, one from a healthy aorta and the other from a healthy internal iliac artery, are used as computational domains. For simplicity, fibers oriented in circumferential and axial directions are considered fixed and only helical fiber orientations ( $\alpha^3, \alpha^4$ ) are considered as variables of anisotropy such that  $\alpha^3 = -\alpha^4$ .

Figure 1 illustrates the convergence history of the objective function and its compartments,  $\mathcal{EG}$  and  $\mathcal{ES}$ , corresponding to Cases 1 and 2 for the aorta model. A sharp decrease in  $\mathcal{EG}$  and a similar reduction in  $\mathcal{ES}$  are noticed for both stress hypotheses when the convergence is achieved. Note that the small plateau regions are associated with the search periods when a new minimum has not been reached yet. Figure 2 contrasts the corresponding optimized distributions of wall thickness and anisotropy for the aorta model in Cases 1 and 2. In both cases, the concave side is found to be relatively thicker than the convex side. Helical fibers on the convex

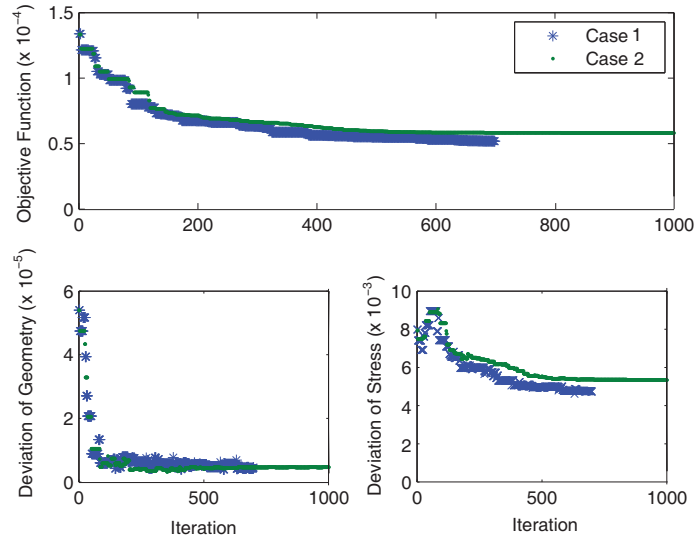


Figure 1: Change in the objective function and its associated compartments versus optimization iterations in Cases 1 and 2 using 60 variables ( $M = 6; N = 5; \xi = 0.01$ ).

side tend to orient themselves more in the circumferential direction as opposed to the concave side, even though the overall anisotropy variation is not as large as the thickness variation. The similar convergence level for both hypotheses (Fig. 1) follows from the similar inhomogeneous distributions of thickness and anisotropy for both cases. In spite of a similar trend of distribution, a larger circumferential anisotropy variation is noticeable in Case 2 (Fig. 2d).

An analogous comparison between Cases 1 and 2 has been made for the internal iliac artery model (Fig. 3). In both cases, relatively similar distributions of wall thickness are observed. However, fiber orientations are distributed with more variability between the two cases than for the aorta model. For the iliac artery model in Case 1, Fig. 4 illustrates the geometric deviation from the *in vivo* configuration ( $\|\mathbf{x} - \mathbf{X}_{image}\|$ ) as well as the normalized deviation of stress in a helical fiber from the homeostatic value ( $(\sigma^k - \sigma_h^k)/\sigma_h^k$ ) when ( $M = 5; N = 3$ ) (a, c) and ( $M = 6; N = 5$ ) (b, d). As expected, the geometric deviation is minimized ( $< 0.3$  mm) in both conditions (Fig. 4a,b).

The maximum deviation of fiber stress from the homeostatic value still seems to be large ( $< 80\%$ ) although on average the deviation has been minimized (Fig. 4c,d). Some adaptive provisions in the optimization may be useful to reduce the localized high values of deviations in future improvements of the proposed technique. Apparently, increasing the number of approximation points (from  $I = 15$  to  $I = 30$ ) in the optimization results in only a minor improvement in reducing the average deviations, while the maximum deviations remains the same. That is, a further increase in approximation points may not be computationally justifiable.

With regard to Case 3, Fig. 5 shows the geometric deviation from the original *in vivo* configuration (a), the normalized deviation of the circumferential cyclic stretch (b) as well as the optimized distributions of wall thickness (c) and anisotropy (d) for the aorta model. As required by the objective function, the geometric deviation from the image is minimized (to a maximum value of 0.05 mm). Cyclic stretch is also homogenized toward the target homeostatic value (i.e., 1.02) on most parts with the largest deviation on areas close to the fixed boundaries (maximum normalized deviation of 1.5%). When compared to Cases 1 and 2 (Fig. 2), lower levels of thickness are predicted by the cyclic stretch hypothesis (Fig. 5c). More circumferential and less longitudinal variations of anisotropy are noticeable in Case 3 (Fig. 5d), whereas anisotropy is more locally distributed in Cases 1 and 2. Convergence of the optimization is an issue when the cyclic stretch hypothesis is applied to a more complex geometry such as the iliac artery model (not shown).

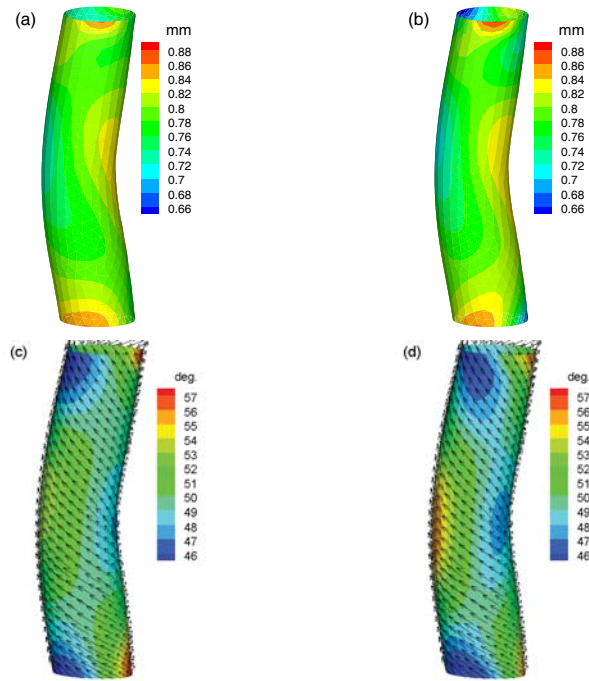


Figure 2: Optimized distributions of thickness (a, b) and anisotropy (c, d) for the aorta model obtained in Cases 1 and 2 ( $M = 6; N = 5; \xi = 0.01$ ). Black arrows identify the direction of one set of corresponding collagen fibers in both Cases 1 and 2 (c, d).

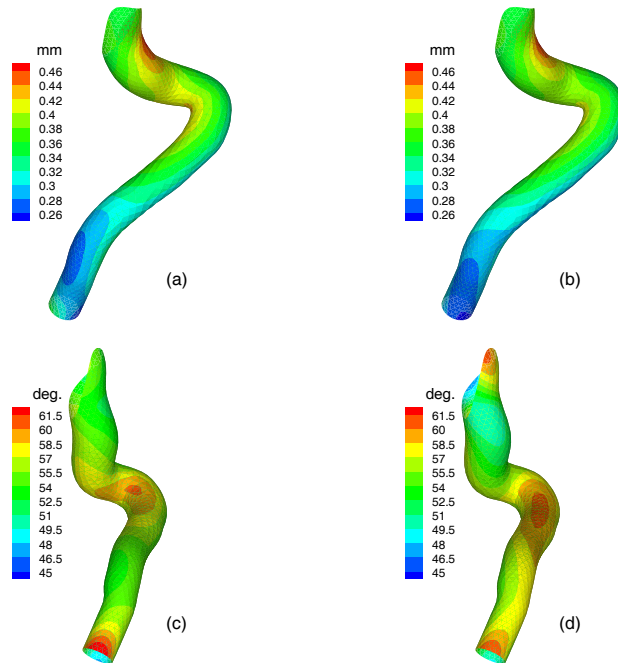


Figure 3: Optimized distributions of thickness (a, b) and anisotropy (c, d) for the internal iliac artery model obtained in Cases 1 and 2 ( $M = 5; N = 3; \xi = 0.1$ ).

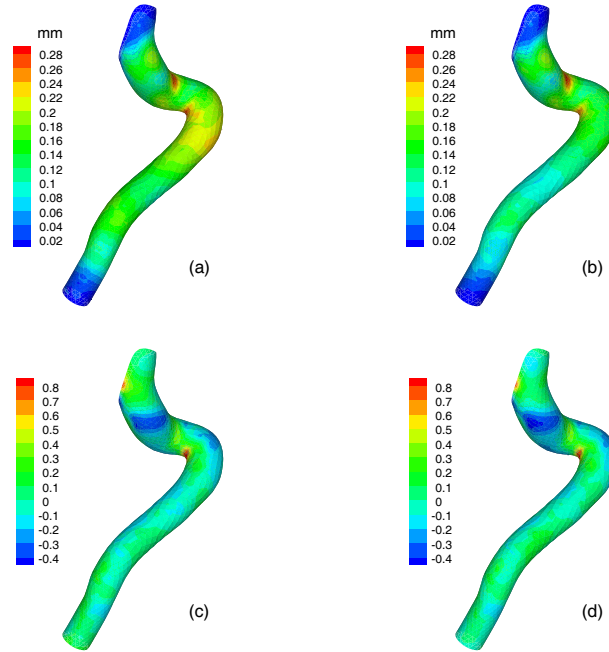


Figure 4: Deviation of the geometry from the *in vivo* configuration ( $\|\mathbf{x} - \mathbf{X}_{image}\|$ ) and deviation of stress in a helical fiber direction from the homeostatic value ( $(\sigma^k - \sigma_h^k)/\sigma_h^k$ ) when ( $M = 5; N = 3$ ) (a, c) and when ( $M = 6, N = 5$ ) (b, d) for the iliac artery model.

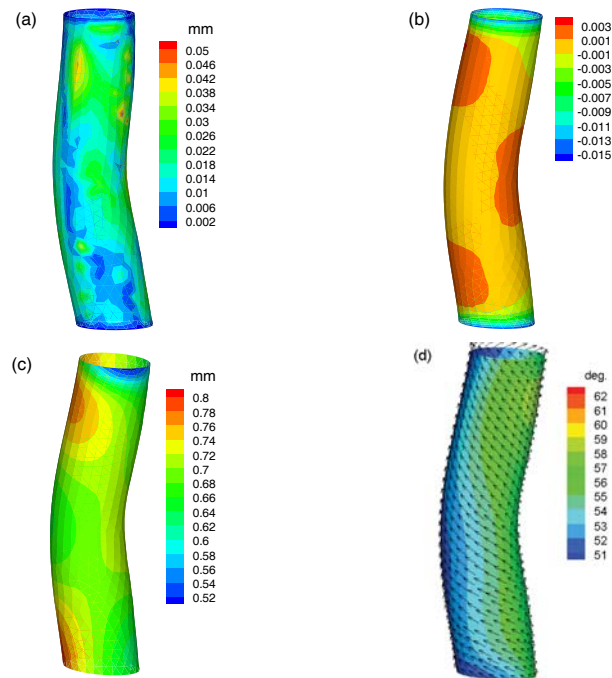


Figure 5: Deviation of the geometry (a), cyclic stretch in circumferential direction ( $\lambda^c$ )(b) and corresponding distributions of thickness and anisotropy (c, d) for the aorta model obtained in Case 3 ( $M = 6; N = 3; \xi = 0.01$ ). Black arrows identify the direction of one set of corresponding collagen fibers (d).

## 5. Discussion

In this study, we utilized a numerical optimization method to find the optimal distributions of structural parameters of healthy arteries based on different homeostatic assumptions (i.e., uniform stress and cyclic stretch). We found that for medical image-based models different homeostatic assumptions lead to different inhomogeneous distributions of wall thickness and anisotropy. The potential application of the proposed optimization method to arteries with higher levels of geometric complexity was also illustrated by using the internal iliac artery model.

Different assumptions for stress homeostasis (Cases 1 and 2) led to homologous overall distributions of thickness, but differing distributions of anisotropy for both arteries (Figs. 2 and 3). Interestingly, the arterial wall on the concave regions was found to be thicker than on the convex regions and the variation of anisotropy was small. Possible correlations between the wall thickness and anisotropy variation and other geometric parameters such as the surface curvature and tortuosity of the vessel wall can be examined in an independent study by systemic application of the technique using multiple image-based arterial geometries. Case 3 (stretch-based homeostasis) produced noticeably contrasting results with Cases 1 and 2. Indeed, in Cases 3, the wall thickness was predicted to be in general smaller than in Cases 1 and 2 (stress-based homeostasis), while a less longitudinal anisotropy variation was observed (Fig. 5). The assumption of a uniform cyclic stretch resulted in a remarkable improvement for both terms of the objective function (Fig. 5a,b), thereby revealing a stronger potential for the cyclic stretch homeostatic assumption, which remains to be further validated with experimental data.

Meanwhile, here, we assumed a constant proportion of the constituents as well as a uniform distribution of the material parameters and focused more on the variation of structural parameters such as the wall thickness and fiber orientation. Some studies, however, indicated non-uniform deformations of the arterial wall during the cardiac cycle (Draney et al., 2004) and observed a circumferential variation of material properties of the aortic wall. In a recent *ex vivo* inflation test of aorta Kim and Baek (2011) found that the posterior region of the arterial wall is thinner, but stiffer than the anterior region. This may be due to the influence of surrounding tissue as well as the local variation in the content of each constituent. Our study excluded the effect of anatomical variation of boundary condition due to the surrounding tissue which may have influenced our results. This effect can be more pronounced when a complex *in vivo* geometry such as the internal iliac artery (Fig. 3) is involved. Also, the fixed boundary conditions considered at both ends are inconsistent with the cyclic stretch homeostatic assumption, thereby resulting in large deviations at both ends (Fig. 5b).

Based on our preliminary results, the error or deviation of geometry relative to the image geometry is less sensitive to the fiber orientations than the wall thickness. Removing the condition  $\alpha_3 = -\alpha_4$  (i.e., adding one more set of optimization variables) did not result in more variability in optimal fiber orientations, whereas it doubled the computational cost. Considering variable orientations for fibers in the axial and circumferential directions greatly adds up to the numerical complexity of the optimization.

It is worth mentioning that the mechanical homeostasis of the normal tissue maintenance may also change under various additional conditions, such as aging and vascular diseases. The application of the current technique to diseased arteries will require more understanding of tissue growth and remodeling under pathological conditions. Nevertheless, the current method showed a distinguishing capability in terms of the optimal structure based on various forms of constitutive relations and homeostatic assumptions. There is a clear need for more experimental data in order to validate and exploit the current technique in understanding the multifactorial process of vascular homeostasis and possible implementation in patient-specific models of vascular diseases.

## 6. Acknowledgements

The authors would like to thank Dr. D.A. Vorp at University of Pittsburgh for providing us with the mechanical test data of human aorta and Dr. C.A. Figueroa at Stanford University for valuable discussions about patient-specific modeling.

## Appendix A. Finite Element Formulation

The arterial wall is considered as a thin membrane, with  $\mathbf{X} = \{X_1, X_2, X_3\}$  and  $\mathbf{x} = \{x_1, x_2, x_3\}$  being the reference and current positions in the global Cartesian coordinate system with base vectors  $\{\mathbf{E}_1, \mathbf{E}_2, \mathbf{E}_3\}$ . Linear triangular elements are used for developing a nonlinear FE model of a non-axisymmetric cylindrical membrane. We define a local Cartesian coordinate system for each element in order to facilitate calculation of the local deformation gradient and prescribe material anisotropy. The centroid of an element  $\mathbf{X}^c = \{X_1^c, X_2^c, X_3^c\}$  is set as the origin of the local Cartesian coordinate system (with base vectors  $\{\mathbf{E}_1^e, \mathbf{E}_2^e, \mathbf{E}_3^e\}$ ) and 'element-wise' orthogonal surface coordinates  $\xi_1$  and  $\xi_2$  are allocated to any point on the element with respect to the origin.

A linear triangular element has three nodal points  $\{\mathbf{X}^{(1)}, \mathbf{X}^{(2)}, \mathbf{X}^{(3)}\}$  in the reference and  $\{\mathbf{x}^{(1)}, \mathbf{x}^{(2)}, \mathbf{x}^{(3)}\}$  in the current configurations while  $X_i^c = \frac{1}{3} \sum_k X_i^{(k)}$  ( $i, k = 1, 2, 3$ ). A set of local orthonormal basis  $\{\mathbf{E}_1^e, \mathbf{E}_2^e, \mathbf{E}_3^e\}$  is then defined on the element with  $\mathbf{X}^c$  as its origin and  $\mathbf{E}_3^e$  being normal to the element. For the reference and current position vectors in the local coordinate system,  $\mathbf{X}^e = \{X_1^e, X_2^e, X_3^e\}$  and  $\mathbf{x}^e = \{x_1^e, x_2^e, x_3^e\}$ , the two-dimensional right Cauchy-Green deformation tensor can be calculated as (Kyriacou et al., 1996; Park and Youn, 1998)

$$\mathbf{C} = \left( \frac{\partial \mathbf{x}^e}{\partial \xi_\alpha} \cdot \frac{\partial \mathbf{x}^e}{\partial \xi_\beta} \right) \mathbf{E}_\alpha^e \otimes \mathbf{E}_\beta^e \quad (\text{A.1})$$

where  $\alpha, \beta = 1, 2$ . The weak form for the membrane is derived from the principle of virtual work

$$\delta I = \int_S \delta w dA - \int_s P \mathbf{n} \cdot \delta \mathbf{x} da = 0, \quad (\text{A.2})$$

where  $P$  is the internal pressure,  $\mathbf{n}$  is the outward normal unit vector. Let a finite approximation of the current position be given as

$$\mathbf{x} = \Phi \mathbf{x}^p, \quad x_i = \Phi_{iA} x_A^p, \quad (\text{A.3})$$

where  $\mathbf{x}^p$  and  $\Phi$  are the nodal vector for the current position and shape function matrix, respectively. The governing equations for an element are derived from the weak form as

$$\{\mathcal{F}\}_P^e = \int_{S^e} \left( \frac{\partial w}{\partial C_{\alpha\beta}} \frac{\partial C_{\alpha\beta}}{\partial x_P^p} - \tilde{P}_i \Phi_{iP} \right) dA = 0, \quad (\text{A.4})$$

where for a linear triangular element,

$$\tilde{P}_i = P \frac{\epsilon_{ijk} (x_j^{(2)} - x_j^{(1)}) (x_k^{(3)} - x_k^{(1)})}{\|\epsilon_{lmn} (X_m^{(2)} - X_m^{(1)}) (X_n^{(3)} - X_n^{(1)})\|}. \quad (\text{A.5})$$

The tangent matrix for the Newton-Raphson method to solve the equation (A.4) is given as

$$\begin{aligned} [\mathbf{K}]_{PQ} &= \left[ \frac{\partial \mathcal{F}}{\partial x^p} \right]_{PQ}^e = \int_{S^e} \left( \frac{\partial^2 w}{\partial C_{\alpha\beta} \partial C_{\gamma\omega}} \frac{\partial C_{\alpha\beta}}{\partial x_P^p} \frac{\partial C_{\gamma\omega}}{\partial x_Q^p} \right. \\ &\quad \left. + \frac{\partial w}{\partial C_{\alpha\beta}} \frac{\partial^2 C_{\alpha\beta}}{\partial x_P^p \partial x_Q^p} - \Phi_{iP} \tilde{P}_{i,Q} \right) dA, \end{aligned} \quad (\text{A.6})$$

where  $(i, j, k, l, m, n = 1, 2, 3)$ ,  $(\alpha, \beta, \gamma, \omega = 1, 2)$ , and  $(A, B, M, P, Q = 1, 2, 3, \dots, 9)$ .

The strain energy  $w$  is the sum of strain energies of all constituents (given by equations (4)-(7)) and is a function of thickness and fiber orientations. At each step of the optimization routine, the calculation of the objective function (equations (8) and (9)) requires the FE solution for the nodal positions and the resulting constituent stress or circumferential stretch with the updated values of thickness and fiber orientations.

## References

- Baek, S., Rajagopal, K. R., Humphrey, J. D., 2006. A theoretical model of enlarging intracranial fusiform aneurysms. *J Biomech Eng*, **128**, 142–149.
- Baek, S., Valentín, A., Humphrey, J. D., 2007. Biochemomechanics of cerebral vasospasm and its resolution: II. constitutive relations and model simulations. *Ann Biomed Eng*, **35**, 1498–1509.
- Boutouyrie, P., Bussy, C., Lacolley, P., Girerd, X., Laloux, B., Laurent, S., 1999. Association between local pulse pressure, mean blood pressure, and large-artery remodeling. *Circulation*, **100**, 1387–1393.
- Cummins, P. M., Sweeney, N. V., Killeen, M. T., Birney, Y. A., Redmond, E. M., Cahill, P. A., 2007. Cyclic strain-mediated matrix metalloproteinase regulation within the vascular endothelium: a force to be reckoned with. *Am J Physiol Heart Circ Physiol*, **292**, H28–H42.
- de Putter, S., Wolters, B. J., Rutten, M. C., Breeuwer, M., Gerritsen, F. A., van de Vosse, F. N., 2007. Patient-specific initial wall stress in abdominal aortic aneurysms with a backward incremental method. *J Biomech*, **40**, 1081–1090.
- Draney, M., Arko, F., Alley, M., R., H., Pelc, N., Zarins, C., Taylor, C., 2004. Quantification of vessel wall motion and cyclic strain 337 using cine phase contrast mri: in vivo validation in the porcine aorta. *Magn Reson Med*, **52**, 286–295.
- Driessen, N. J. B., Cox, M. A. J., Bouten, C. V. C., Baaijens, F. P. T., 2008. Remodelling of the angular collagen fiber distribution in cardiovascular tissues. *Biomech Model Mechanobiol*, **7**, 93103.
- Eberth, J. F., Gresham, V. C., Reddy, A. K., Popovic, N., Wilson, E., Humphrey, J. D., 2009. Importance of pulsatility in hypertensive carotid artery growth and remodeling. *J Hypertens* **27**, 2010–2021.
- Figueroa, C. A., Baek, S., Taylor, C. A., Humphrey, J. D., 2009. A computational framework for fluid-solid-growth modeling in cardiovascular simulations. *Comput Methods Appl Mech Eng*, **198**, 3583–3602.
- Gee, M. W., Reeps, C., Eckstein, H. H., Wall, W. A., 2009. Prestressing in finite deformation abdominal aortic aneurysm simulation. *J Biomech*, **42**, 1732–1739.
- Gleason, R. L., Humphrey, J. D., 2004. A mixture model of arterial growth and remodeling in hypertension: Altered muscle tone and tissue turnover. *J Vasc Surg*, **41**, 352–363.
- Gleason, R. L., Taber, L. A., Humphrey, J. D., 2004. A 2-d model of flow-induced alterations in the geometry, structure, and properties of carotid arteries. *J Biomech Eng*, **126**, 371–381.
- Guo, X. M., Kassab, G. S., 2004. Distribution of stress and strain along the porcine aorta and coronary arterial tree. *Am J Physiol Heart Circ Physiol*, **286**, H2361–H2368.
- Hansen, L., Wan, W., Gleason, R. L., 2009. Microstructurally motivated constitutive modeling of mouse arteries cultured under altered axial stretch. *J Biomech Eng*, **131**, 101015.
- Hariton, I., deBotton, G., Gasser, T. C., Holzapfel, G. A., 2007. Stress-driven collagen fiber remodeling in arterial walls. *Biomech Model Mechanobiol*, **6**, 163–175.
- Hsu, H.-J., Lee, C.-F., Kaunas, R., 2009. A dynamic stochastic model of frequency-dependent stress fiber alignment induced by cyclic stretch. *PLoS ONE*, **4**, e4853.
- Humphrey, J. D., 2001. Stress, strain, and mechanotransduction in cells. *J Biomech Eng*, **123**, 638–641.
- Humphrey, J. D., 2002. Cardiovascular Solid Mechanics: Cells, Tissues, and Organs. Springer-Verlag, New York.

- Humphrey, J. D., Rajagopal, K. R., 2002. A constrained mixture model for growth and remodeling of soft tissues. *Math Models Methods Appl Sci*, **12**, 407–430.
- Humphrey, J. D., Wells, P., Baek, S., Hu, J.-J., McLeroy, K., Yeh, A., 2008. A theoretically-motivated biaxial tissue culture system with intravital microscopy. *Biomech Model Mechanobiol*, **7**, 323–334.
- Kamiya, A., Togawa, T., 1980. Adaptive regulation of wall shear-stress to flow change in the canine carotid-artery. *Am J Physiol*, **239**, H14–H21.
- Kassab, G. S., 2008. Mechanical homeostasis of cardiovascular tissue. In: Artmann, G. M., Chien, S. (Eds.), *Bioengineering in Cell and Tissue Research*. Springer, pp. 371–391.
- Kim, J., Baek, S., 2011. Circumferential variations of mechanical behavior of the porcine thoracic aorta during the inflation test. *J Biomech*, (in print)-DOI: 10.1016/j.jbiomech.2011.04.022.
- Kyriacou, S. K., Schwab, C., Humphrey, J. D., 1996. Finite element analysis of nonlinear orthotropic hyperelastic membranes. *Comput Mech* **18**, 269–278.
- Lagarias, J. C., Reeds, J. A., Wright, M. H., Wright, P. E., 1998. Convergence properties of the nelder-mead simplex method in low dimensions. *SIAM J Optim*, **9**, 112–147.
- Langille, B. L., Bendeck, M. P., Keeley, F. W., 1989. Adaptation of carotid arteries of young and mature rabbits to reduced carotid blood-flow. *Am J Physiol*, **256**, H931–H939.
- Leung, D. Y. M., Glagov, S., Mathews, M. B., 1976. Cyclic stretching stimulates synthesis of matrix components by arterial smooth-muscle cells invitro. *Science*, **191**, 475–477.
- Lillie, M. A., Gosline, J. M., 2007. Mechanical properties of elastin along the thoracic aorta in the pig. *J Biomech*, **40**, 2214–2221.
- Lu, J., Zhou, X., Raghavan, M. L., 2007. Inverse elastostatic stress analysis in pre-deformed biological structures: Demonstration using abdominal aortic aneurysms. *J Biomech*, **40**, 693–696.
- Lu, X., Zhao, J. B., Wang, G. R., Gregersen, H., Kassab, G. S., 2001. Remodeling of the zero-stress state of femoral arteries in response to flow overload. *Am J Physiol Heart Circ Physiol*, **280**, H1547–H1559.
- Matsumoto, T., Hayashi, K., 1994. Mechanical and dimensional adaptation of rat aorta to hypertension. *J Biomech Eng*, **116**, 278–283.
- McKnight, N. L., Frangos, J. A., 2003. Strain rate mechanotransduction in aligned human vascular smooth muscle cells. *Ann Biomed Eng*, **31**, 239–249.
- Park, H. C., Youn, S., 1998. Finite element analysis and constitutive modelling of anisotropic nonlinear hyperelastic bodies with convected frames. *Comput Methods Appl Mech Eng* **151**, 605–618.
- Sheidaei, A., Hunley, S. C., Zeinali-Davarani, S., Raguin, L. G., Baek, S., 2011. Simulation of abdominal aortic aneurysm growth with updating hemodynamic loads using a realistic geometry. *Med Eng Phys*, **33**, 80–88.
- Speelman, L., Bosboom, E. M. H., Schurink, G. W. H., Buth, J., Breeuwer, M., Jacobs, M. J., van de Vosse, F. N., 2009. Initial stress and nonlinear material behavior in patient-specific aaa wall stress analysis. *J Biomech*, **42**, 1713–1719.
- Torczon, V. J., 1989. Multi-directional search: A direct search algorithm for parallel machines. Ph.D. thesis, Rice University.
- Valentín, A., Cardamone, L., Baek, S., Humphrey, J. D., 2009. Complementary vasoactivity and matrix remodeling in arterial adaptations to altered flow and pressure. *J R Soc Interface*, **6**, 293–306.

- Vande Geest, J. P., Sacks, M. S., Vorp, D. A., 2004. Age dependency of the biaxial biomechanical behavior of human abdominal aorta. *J Biomech Eng*, **126**, 815–822.
- Vande Geest, J. P., Sacks, M. S., Vorp, D. A., 2006. The effects of aneurysm on the biaxial mechanical behavior of human abdominal aorta. *J Biomech*, **39**, 1324–1334.
- Wan, W., Hansen, L., Gleason, R. L., 2010. A 3-d constrained mixture model for mechanically mediated vascular growth and remodeling. *Biomech Model Mechanobiol*, **9**, 403–419.
- Watton, P. N., Hill, N. A., 2009. Evolving mechanical properties of a model of abdominal aortic aneurysm. *Biomech Model Mechanobiol*, **8**, 25–42.
- Wolinsky, H., 1971. Effects of hypertension and its reversal on thoracic aorta of male and female rats - morphological and chemical studies. *Circ Res*, **28**, 622–637.
- Xu, C. P., Zarins, C. K., Bassiouny, H. S., Briggs, W. H., Reardon, C., Glagov, S., 2000. Differential transmural distribution of gene expression for collagen types i and iii proximal to aortic coarctation in the rabbit. *J Vasc Res*, **37**, 170–182.
- Zeinali-Davarani, S., Choi, J., Baek, S., 2009. On parameter estimation for biaxial mechanical behavior of arteries. *J Biomech*, **42**, 524–530.
- Zeinali-Davarani, S., Raguin, L. G., Vorp, D. A., Baek, S., 2011a. Identification of in vivo material and geometric parameters of a human aorta: toward patient-specific modeling of abdominal aortic aneurysm. *Biomech Model Mechanobiol*, (in print)-DOI: 10.1007/s10237-010-0266-y.
- Zeinali-Davarani, S., Sheidaei, A., Baek, S., 2011b. A finite element model of stress-mediated vascular adaptation: application to abdominal aortic aneurysms. *Comput Methods Biomech Biomed Eng*, (in print)-DOI: 10.1080/10255842.2010.495344.